

Fast γ -ray variability in blazars beyond redshift 3

Shang Li^{1,2}, Zi-Qing Xia¹, Yun-Feng Liang¹, Neng-Hui Liao¹, Yi-Zhong Fan¹

liaonh@pmo.ac.cn

yzfan@pmo.ac.cn

ABSTRACT

High-redshift blazars are one of the most powerful monsters in the universe and γ -ray variability carries crucial information of their relativistic jets. In this work we present results of the first systematical temporal analysis of *Fermi*-LAT data of all known seven γ -ray blazars beyond redshift 3. Significant long-term γ -ray variability is found from five sources in monthly γ -ray light curves, in which three of them are reported for the first time. Furthermore, intraday γ -ray variations are detected from NVSS J053954–283956 and NVSS J080518+614423. Doubling variability timescale of the former source is limited as short as $\lesssim 1$ hour (at the source frame). Together with variability amplitude over one order of magnitude, NVSS J053954–283956 is the most distant γ -ray flaring blazar so far. Meanwhile, intraday optical variability of NVSS J163547+362930 is found based on archival PTF/iPTF light curve. Benefited from multiwavelength activity of these sources, constraints of their Doppler factors as well as locations of γ -ray radiation region and indications for the SDSS high redshift jetted active galactic nuclei deficit are discussed.

Subject headings: galaxies: active – galaxies: high-redshift – galaxies: jets – gamma rays: galaxies – quasars: general – radiation mechanisms: non-thermal

1. Introduction

Blazars, including flat spectrum radio quasars (FSRQs) and BL Lacertae objects (BL Lacs), are radio-loud active galactic nuclei (AGNs) whose relativistic jets are closely pointing

¹Key Laboratory of Dark Matter and Space Astronomy, Purple Mountain Observatory, Chinese Academy of Sciences, Nanjing 210008, China

²University of Chinese Academy of Sciences, Yuquan Road 19, Beijing 100049, China

to our line of sight (Blandford & Rees 1978; Urry & Padovani 1995). The jet viewing angle θ_v is smaller than or comparable to the jet beaming angle ($1/\Gamma$, where Γ is the jet bulk Lorentz factor), hence the jet emission is strongly boosted because of relativistic effects, making blazars so luminous that they are visible even at very high redshifts (e.g., Romani et al. 2004; Yi et al. 2014). High-redshift blazars are extremely powerful monsters harboring super-massive black holes (SMBHs) heavier than one billion solar masses (e.g., Ghisellini et al. 2010). These sources are of major importance since they shed lights on formation and growth of the first generation of SMBHs and the role that relativistic jets play at that time (e.g., Volonteri 2010; Afonso et al. 2015). Studies of high-redshift blazars also provide information on whether and how the jet properties change with cosmic time, along with their potential impact on evolution of AGNs as well as their host galaxies (e.g., Fabian 2012; Volonteri et al. 2011; Morganti et al. 2013).

Since the relativistic jets are responsible for bright radiation of blazars, they are characterized by highly variable and polarized nonthermal continuum emissions, generally detected in all observable bands from radio to γ -ray (both GeV and TeV) regimes (Ulrich et al. 1997). Their spectral energy distribution (SED) reveals a two-bump shape, where one is likely due to synchrotron emission of relativistic electrons in magnetic fields and the other extending to γ rays is usually explained as inverse Compton scattering of soft photons by the same population of relativistic electrons (e.g., Maraschi et al. 1992; Dermer & Schlickeiser 1993; Sikora et al. 1994; Błażejowski et al. 2000). One of the extraordinary phenomena in blazars is their fast γ -ray variability. Imaging atmospheric Cerenkov telescopes (IACTs), like HESS and MAGIC, have detected flux changes on a time scale of a few minutes in high frequency peaked BL Lacs PKS 2155–304 (Aharonian et al. 2007) and Mkn 501 (Albert et al. 2007). Similar extreme behaviors have been also detected in other subtypes of jetted AGNs, including the low frequency peaked BL Lac BL Lacertae (Arlen et al. 2013) and FSRQ PKS 1222+21 (Aleksić et al. 2011), strongly suggesting it is a common feature independent on the source type. In GeV domain, flux variations on a time scale of several hours have been found in a few sources since the CGRO era (e.g., Mattox et al. 1997; Wehrle et al. 1998). Number of such detections has significantly increased right now thanks to the latest generation of space γ -ray telescope *Fermi*, though the minimum variability timescale is generally limited to a few hours due to its routine survey observation mode (e.g., Foschini et al. 2011; Vovk & Neronov 2013; Liao & Bai 2015; Liao et al. 2016, but also see Foschini et al. 2013). Recently, taking advantage of a target of opportunity (ToO) repointing of *Fermi* Large Area Telescope (LAT, Atwood et al. 2009), extremely fast GeV γ -ray flux variability with doubling time less than 5 minutes has been detected in a giant outburst of 3C 279 (Ackermann et al. 2016). Fast γ -ray variability of blazars is important for investigating the speed, composition and energetics of relativistic jets (e.g., Begelman et al. 2008).

Detected number of high redshift blazar candidates (i.e. $z \gtrsim 4$) has significantly increased over the last decade, thanks to unprecedentedly powerful X-ray observatories (e.g. *Swift*; Gehrels et al. 2004) as well as wide-field surveys in the optical/UV (e.g. the Sloan Digital Sky Survey, SDSS; York et al. 2000), infrared (*WISE*; Wright et al. 2010), and radio bands (e.g. the NRAO VLA Sky Survey, NVSS; Condon et al. 1998). So far the farthest known blazar candidate is Q0906+6930 ($z = 5.48$; Romani et al. 2004), along with several others beyond redshift 5, including SDSS J102623.61+254259.5 ($z = 5.2$; Sbarrato et al. 2012), SDSS J013127.34–032100.1 ($z = 5.18$; Yi et al. 2014) and SDSS J114657.79+403708.6 ($z = 5.0$; Ghisellini et al. 2014). These sources are identified as blazars in consideration of their high radio loudness and hard X-ray spectra (e.g., Romani 2006). In γ -ray perspective, all γ -ray AGNs beyond redshift 3 are FSRQs and PKS 0537–286 ($z = 3.1$; Wright et al. 1978) had stood as the farthest γ -ray blazar for a long time (Abdo et al. 2010a). Recently, 5 new γ -ray blazars with redshifts over 3.3 have been identified by *Fermi*-LAT Collaboration based on spatially overlapping between the γ -ray sources and their optical counterparts as well as their typical γ -ray FSRQ shape SEDs (i.e. high Compton dominance; Ackermann et al. 2017). However, variability information of these sources is still lacking.

Here we perform a detailed analysis of *Fermi*-LAT γ -ray data of all known 7 γ -ray blazars beyond redshift 3. This work is organized as follows: in section 2, strategies in the *Fermi*-LAT data analysis procedure is introduced; results of the analysis are reported in section 3, in which we mainly focus on the results in the temporal domain; finally, in section 4 we summarize our results with some discussions.

2. LAT DATA ANALYSES

In this paper, we used publicly released *Fermi*-LAT Pass 8 data (P8R2_SOURCE_V6, FRONT+BACK) and updated *Fermi Science-Tools* package of version v10r0p5 to perform the analysis. For each target, we considered the data set within a 10° region of interest (ROI) from 2008 October 27 to 2017 June 12 (i.e., Mission Elapsed Time, MET, between 246823875 s and 518983875 s), along with energy range from 100 MeV to 100 GeV. In order to reduce contamination from the Earth’s limb, we removed γ -ray events with zenith angle larger than 90° . The recommended quality-filter cuts (i.e. DATA_QUAL==1 && LAT_CONFIG==1) have been followed to ensure that the spacecraft keeps in a good condition and hence the data set is valid for science use.

Firstly, we used the script `make3FGLxml.py`¹ to generate an initial background model

¹<http://fermi.gsfc.nasa.gov/ssc/data/analysis/user/>

for each target, which includes all point source within 15° in the third *Fermi*-LAT source catalog (3FGL) (Acero et al. 2015) as well as the latest galactic diffuse γ -ray emission model `gll_iem_v06.fits` and isotropic emission template `iso_P8R2_SOURCE_V6.v06.txt`² (Acero et al. 2016). γ -ray locations and spectral templates (i.e. power-law function, $dN/dE \propto E^{-\Gamma}$, where Γ is the spectral index) of the targets were set same as that in the literature (Acero et al. 2015; Ackermann et al. 2017). Then unbinned likelihood algorithm implemented in the `gtlike` task was adopted to extract the flux and spectrum. During the extraction, the flux and spectral parameters of sources within the 10° ROI, together with normalization factors of the two diffuse components, were set free. Significance of the target is quantified with the test statistic (TS), defined as $TS = -2\ln(L_0/L)$ (Mattox et al. 1996), where L and L_0 are the maximum likelihood values for the model with and without target source, respectively. Since 3FGL is based on 4-year *Fermi*-LAT data that has narrower data time range than ours, we have checked whether there are newly emerging γ -ray sources beyond 3FGL by generating a residual TS map for each ROI. All new γ -ray background sources corresponding to excesses with $TS > 25$ (i.e. detection significance of 4.2σ) in the TS maps were added into the background model. For these new sources, their spectral models were also set to be power-law function and γ -ray positions were obtained by the `gtfindsrc` task. After all these steps, the final results were obtained by analyzing the updated background model.

In temporal analysis, for background sources neither bright (i.e. TS value twice that of the target) nor close ($< 4^\circ$) to the targets, their spectral indexes were frozen to values from the global fit. Meanwhile, considering high Galactic latitude background point sources that are dominated by blazars with highly variable γ -ray emissions, we removed the weak background sources (i.e. $TS < 1$) from the source model. When a special γ -ray flare event was focused, firstly, an analysis of the entire flare epoch (i.e. several tens of days) was performed. Then short-term light curves were extracted to search evidences of intraday γ -ray variability. During the extraction, normalizations of two diffuse emission components and spectral parameters of all background sources were fixed to values from the analysis covering the whole flaring period. Note that this strategy has been also adopted for several similar studies (e.g., Saito et al. 2013; Liao & Bai 2015; Liao et al. 2016; Ackermann et al. 2016). Meanwhile, we also took into account the ϕ dependence of effect area of *Fermi*-LAT due to its square shape, and set `phibins=5` in the `gtlrcube` task then. When TS value of the target is smaller than 4, `pyLikelihood UpperLimits` tool was adopted to calculate the 95% upper limit of the flux.

²<http://fermi.gsfc.nasa.gov/ssc/data/access/lat/BackgroundModels.html>

3. RESULTS

3.1. Global analysis

There are in total 7 known γ -ray blazars beyond redshift 3 so far. Their basic information are listed in Table 1. Two sources (i.e. NVSS J053954–283956 and NVSS J080518+614423) are known as relatively strong γ -ray sources and have been included in *Fermi* source catalogs (e.g., Abdo et al. 2010b; Acero et al. 2015). γ -ray emissions of other five sources have been detected from a recent search of high redshift γ -ray blazars performed by *Fermi* collaboration (Ackermann et al. 2017). Redshift range of these 7 sources is between 3.0 and 4.3, especially NVSS J151002+570243 locates beyond redshift 4. Except NVSS J053954–283956 whose SMBH mass listed here is obtained from modeling its big blue bump from the accretion disk (Ghisellini et al. 2010), other estimations are based on optical spectroscopic observations (Torrealba et al. 2012; Alam et al. 2015).

Before performing the temporal analysis, a fit of the entire ~ 105 months LAT data for each source has been accomplished. All 7 sources are found as significant γ -ray emitters with soft spectra (i.e. $\Gamma_\gamma > 2.7$), which is consistent with the literature (Acero et al. 2015; Ackermann et al. 2017). Averaged γ -ray fluxes as well as corresponding γ -ray spectral indexes and TS values are also provided in Table 1. NVSS J053954–283956 is the brightest one among these sources, along with the highest TS value. Note that for sources selected from Ackermann et al. (2017), our averaged fluxes are generally lower than their values, because we chose a different energy range of LAT data (i.e. 0.1 GeV – 100 GeV) from theirs (i.e. 0.06 GeV – 300 GeV). For sources with TS > 100 , sophisticated spectral model (i.e. Log-parabolic function) is adopted to fit the entire LAT data, but no significant improvement is found compared to the initial usage of powerlaw function.

3.2. Temporal behaviors

3.2.1. Monthly γ -ray light curves

Since majority of our sources are not bright in γ rays (i.e. $\text{TS}_{105 \text{ month}} \lesssim 100$), firstly, we evenly divide the total LAT data into 21 time bins (with each bin about 5 months) to extract a γ -ray light curve for each source, see Figure 1. For NVSS J053954–283956 and NVSS J080518+614423, significant γ -ray variability is obvious, confirming the results in *Fermi* source catalogs (e.g., Nolan et al. 2012). While for other five sources, their error bars are relatively large and there are many upper limits in the light curves. So we use “variability index” test (Nolan et al. 2012) to quantify significance of variability of the light curves, from

which information of the upper limits can be properly considered. The null hypothesis of this test is that source flux is constant across the full time period. The variability index is derived using following expression in Nolan et al. (2012),

$$\text{TS}_{\text{var}} = -2 \sum_i \frac{\Delta F_i^2}{\Delta F_i^2 + f^2 F_{\text{const}}^2} \ln \left(\frac{\mathcal{L}_i(F_{\text{const}})}{\mathcal{L}_i(F_i)} \right), \quad (1)$$

where for the i -th time bin, \mathcal{L}_i is the likelihood value, F_i is the observed photon flux, ΔF_i is the statistical uncertainty of F_i , F_{const} is the assumed constant flux, and f is the systematic correction factor which we take a value of 2% following Nolan et al. (2012). In our analysis, the optimized constant flux for each source is close to the average flux from the global analysis (within 1σ statistical uncertainty). If the null hypothesis is correct, the derived TS_{var} in case of a light curve with 21 time bins should follow a χ^2 distribution with 20 degrees of freedom and hence the variability significance in σ unit is obtained (also listed in Table 1). It is not surprised that σ_{var} values of NVSS J053954–283956 and NVSS J080518+614423 are high (i.e. > 10). Interestingly, we find γ -ray emissions of NVSS J135406–020603, NVSS J151002+570243 and NVSS J163547+362930 are significantly variable (i.e. $\sigma_{\text{var}} > 3$). Due to the limited angular resolution of *Fermi*-LAT strong variability in nearby background sources can cause artificial variability for the target. Therefore, we have checked whether there are any such neighbors around these five sources. We find that this situation only happens to NVSS J163547+362930, for which there is one bright and highly variable background source 3FGL J1635.2+3809 about 1.6° away. Since the 68% C.L. contamination angle of LAT for 500 MeV photons is about 1.5° , to avoid significant impact from the neighbor, individual light curves with lower energy cut of LAT data raising from 100 MeV to 500 MeV both for the target and the neighbor are extracted (see Figure 2). There are two major γ -ray flares in the > 100 MeV light curve of NVSS J163547+362930, with peaking time around MJD 56192 and MJD 56792, respectively. The former flare coincides with a high flux state of the neighbor 3FGL J1635.2+3809 and disappears in the > 500 MeV light curve, indicating that it is probably artificial. However, the other flare corresponds to a low flux state of the neighbor and remains to be significant in the > 500 MeV light curve, which suggests an intrinsic link between this flare and the target. Variability index of the > 500 MeV light curve of NVSS J163547+362930 is also calculated, given as $\sigma_{\text{var}} = 4.9$. Although it is smaller than that in > 100 MeV case, the γ -ray emission of NVSS J163547+362930 is still proved to be significantly variable.

3.2.2. Detecting fast γ -ray variability

According to the monthly γ -ray light curves, fluxes of several time bins are significantly higher than the averaged flux. Together with relatively large TS values (i.e. > 50), it allows us to further search for any possible fast γ -ray variability. Except for NVSS J135406-020603 that no significant variability in short-term is found, detailed temporal analyses of NVSS J053954–283956, NVSS J080518+614423 and NVSS J163547+362930 are described below.

NVSS J053954–283956

NVSS J053954–283956, also named as PKS 0537–286, is one of the most luminous high-redshift quasars ($z=3.104$, [Wright et al. 1978](#)). Its first detection was at radio frequencies (e.g., [Bolton et al. 1975](#)). It is also a bright and well-studied source in X rays (e.g., [Zamorani et al. 1981](#); [Sambruna et al. 2007](#); [Bottacini et al. 2010](#)), showing an extremely high X-ray luminosity ($\sim 10^{47}$ erg s^{-1} in the 0.1-2 keV range) and a particularly hard spectrum ($\Gamma_X \sim 1.2$), indicative of a significant contribution of the nonthermal jet emission. In temporal perspective, modest optical-NIR and X-ray continuum variations have been observed ([Bottacini et al. 2010](#)). Here we present its γ -ray temporal characteristics. As shown in the monthly γ -ray light curve of NVSS J053954–283956 (Figure 1), there are three γ -ray flares. Enlarged 15-day and 3-day time bin γ -ray light curves corresponding to these flares are presented in Figure 3. For the first two flares (i.e. flare-A and flare-B), no significant intraday γ -ray variability are found, confirming a previous study that suggests a minimum γ -ray variability timescale of ~ 18 days then ([Vovk & Neronov 2013](#)). However, the third flare (i.e. flare-C) detected in May 2017³, exhibits a totally different behavior. In the 15-day time bin light curve of the flare-C, flux of the eighth bin is significantly higher than the averaged flux, whereas the target maintains in the low flux state for the rest of time. Moreover, such a behavior is confirmed by the further 3-day time bin γ -ray light curve, where an intense γ -ray outburst suddenly appears. The flux quickly rises to the maximum value within about 6 days (1.46 days at the source frame) and the descent time is as short as the ascent time. In addition to the short variability timescale, variation amplitude of this outburst is one order of magnitude larger than the average flux. The 3-day peaking flux reaches to $(1.2 \pm 0.1) \times 10^{-6}$ ph $cm^{-2} s^{-1}$ with a very high TS value ($\simeq 426$), while averaged fluxes in epoch of flare-C and entire 105 months are $(1.0 \pm 0.1) \times 10^{-7}$ ph $cm^{-2} s^{-1}$ and $(4.9 \pm 0.2) \times 10^{-8}$ ph $cm^{-2} s^{-1}$, respectively. These results put a tight constraint on the doubling timescale at the source frame, $\tau_{doub,source} = \Delta t \times \ln 2 / \ln(F_1/F_2) / (1+z) < 0.5$ day. Powerlaw function provides an acceptable description to the burst SED while log-parabolic function does not bring any

³This flare event has also been reported in ATel by *Fermi* collaboration ([Cheung et al. 2017](#)).

significant improvements. Spectral index of the burst SED ($\Gamma=2.53\pm 0.09$) is slightly harder than the averaged SED ($\Gamma=2.78\pm 0.04$), consistent with [Cheung et al. \(2017\)](#). Meanwhile, following γ -ray localization analysis gives that the optimized location at this time is R.A. 85.04° and DEC. -28.64° . The corresponding 95% C.L. error radius is 0.10° which is consistent with the value (0.08°) listed in 3FGL ([Acero et al. 2015](#)). Since the angular separation between the γ -ray position and radio location of NVSS J053954–283956 is 0.06° , it still locates within the 95% C.L. error radius. Note that in the normal observation mode LAT performs a complete and uniform coverage of the sky in 3-hr, thus we limit the minimum time bin in our analysis to 3-hr. Therefore, 12-hr, 6-hr and 3-hr time bin γ -ray light curves are extracted to perform further investigations, see Figure 4. Since in the epoch of flare-C the target is at a high flux state that most of the time bins are not upper limits, we adopt a simple χ^2 test to check whether the source is significantly variable. By optimizing the assuming constant flux, we find evidences of significant variability on intraday γ -ray light curves, $(p, \chi^2/\text{dof}) = (7.0 \times 10^{-8}, 61.4/14)$ for 12-hr light curve and $(1.6 \times 10^{-5}, 65.7/25)$ for 6-hr light curve, respectively. However, variability for 3-hr light curve is not statistically significant due to large uncertainties, $(p, \chi^2/\text{dof}) = (0.11, 26.7/19)$. Variability timescales are also estimated (listed in Table 2) by fitting data in the ascent phase with the exponential function:

$$F(t) = F(t_0) \cdot 2^{-(t-t_0)/\tau}, \quad (2)$$

where $F(t)$ and $F(t_0)$ are the fluxes at time t and t_0 , respectively, and τ is the characteristic time scale. In the 12-hr light curve, a quick raise begins in the sixth time bin (i.e. at MJD 57877.5, with a flux of $(4.3 \pm 1.6) \times 10^{-7}$ ph cm $^{-2}$ s $^{-1}$), one day later the flux reaches the peak (i.e. at MJD 57878.5, $(1.6 \pm 0.3) \times 10^{-6}$ ph cm $^{-2}$ s $^{-1}$). Since the eighth time bin, the target maintains in a high flux state ($\gtrsim 10^{-6}$ ph cm $^{-2}$ s $^{-1}$) but with a relatively modest descent that costs about 2.5 days, then the target is back to a quiescent flux state. This variability trend is confirmed by the 6-hr light curve, from which the ascent time is constrained as 18-hr (as short as 4.4-hr at the source frame). Together with the variation amplitude (i.e. $F_{\text{bin15}}/F_{\text{bin12}} \simeq 8.4$), $\tau_{\text{doub,source}}$ can be estimated as short as 1.4-hr. A similar $\tau_{\text{doub,source}}$ (i.e. 1.3-hr) can be also derived from the ascent phase in 3-hr light curve despite the large error bars. Meanwhile, the 6-hr light curve reveals that the entire outburst may constitute of several sub-flares. Interestingly, violent variability may appear in these sub-flares. For example, in 3-hr light curve the flux raises from $(3.8 \pm 2.7) \times 10^{-7}$ ph cm $^{-2}$ s $^{-1}$ at MJD 57879.70 to $(2.5 \pm 0.9) \times 10^{-6}$ ph cm $^{-2}$ s $^{-1}$ at MJD 57879.82, leading to a very short variability timescale of $\tau_{\text{doub,source}} \sim 16$ -min.

NVSS J080518+614423

NVSS J080518+614423 ($z=3.033$, [Sowards-Emmerd et al. 2005](#)) was also firstly known as radio emitters ([Becker et al. 1991](#)), then its optical counterpart was identified ([Snellen et al. 2002](#)). Similar with NVSS J053954–283956, it has been detected by *WISE* and *Swift*-BAT ([D’Abrusco et al. 2012](#); [Baumgartner et al. 2013](#)). In its monthly γ -ray light curve, after two flares (i.e. flare-A and flare-B) in the first and second year of *Fermi* observation, it maintains at a low flux state for several years. These two flares are confirmed by enlarged 15-day time bin γ -ray light curves, see Figure 5. More importantly, an evidence of intraday γ -ray variability is found from the 3-day time bin γ -ray light curve of flare-A, of which the variability index is given as $\sigma_{var} = 10.8\sigma$. But no similar behavior can be found in flare-B due to large uncertainties, also see Figure 5. In consideration of the ascent time of 6 days, together with the variability amplitude of 3.5, the intrinsic doubling timescale in flare-A can be estimated as $\tau_{doub,source} \simeq 19.6$ -hr. Note that the 3-day peaking flux ($(3.9 \pm 0.7) \times 10^{-7}$ ph cm $^{-2}$ s $^{-1}$) is roughly 15 times of the 105 months averaged flux. Intraday γ -ray light curves (i.e. 12-hr and 5-hr time bins) corresponding to this epoch have been also extracted, see Figure 6, no further constraints of the variability timescale are obtained. Similar with NVSS J053954–283956, the spectral index in flare-A of NVSS J080518+614423 ($\Gamma=2.40 \pm 0.12$) is harder than the averaged SED ($\Gamma=2.82 \pm 0.05$). Meanwhile, the optimized γ -ray position at this time is R.A. 121.25° and DEC. 61.73° with 95% C.L. error radius of 0.12°. The angular separation between the γ -ray position and radio position of NVSS J080518+614423 is only 0.04°, supporting the association.

NVSS J163547+362930

NVSS J163547+362930 was discovered by the MIT-Green Bank 5 GHz survey ([Griffith et al. 1990](#)). Then it has been included in the DR10 SDSS quasar catalog, with a redshift estimation of 3.647 ([Pâris et al. 2014](#)). As shown in Figure 2, there is a flare in the monthly > 500 MeV γ -ray light curve of NVSS J163547+362930 which is probably not from the neighbor. Therefore, an enlarged 15-day time bin > 500 MeV light curve has been extracted, together with another one of the neighbor 3FGL J1635.2+3809, see Figure 7. Interestingly, though the variability at the overall period is not significant (i.e. $\sigma_{var} = 1.5\sigma$) due to large uncertainties, flux of the tenth bin (TS = 39) is roughly three times of the averaged flux during this epoch. While the neighbor is not detectable (TS < 4) for *Fermi*-LAT at the same time, confirming what we find in the monthly light curve. The optimized γ -ray location for this time bin is R.A.= 248.89° and Dec.= 36.46°. Since the angular separation is 0.06° while the 95% C.L. γ -ray error radius of is 0.10°, the association between NVSS J163547+362930 and the γ -ray source is confirmed. Similar with former two sources, a sign of

bluer-when-brighter spectral variability behavior has been found for NVSS J163547+362930 (i.e. $\Gamma_{\text{flare}, > 500 \text{ MeV}} = 2.58 \pm 0.25$ while $\Gamma_{105 \text{ month}, > 500 \text{ MeV}} = 2.73 \pm 0.23$). From the 15-day light curve, intrinsic doubling timescale can be constrained as ~ 2.2 and 1.4 days for the ascend and descend phase, respectively. Unfortunately, no evidences of intraday γ -ray variability are found in further temporal analyses.

4. SUMMARY AND DISCUSSIONS

Benefited from large effective area and wide field of view of *Fermi*-LAT, together with its routine survey mode covering the entire sky in every 3-hr, our understanding of γ -ray variability properties of blazars has been profoundly improved. Significant γ -ray variability has been accepted as a common feature of γ -ray blazars, with variability amplitude up to more than two orders of magnitudes and variability timescale ranging from minutes to years (e.g., Nolan et al. 2012; Liao & Bai 2015; Liao et al. 2016; Ackermann et al. 2016). In long-term, evidences of quasi-periodic modulation of γ -ray emission of several blazars have been reported (e.g., Ackermann et al. 2015; Zhang et al. 2017). In addition to flux variation alone, changes of γ -ray spectrum are often observed during different flux statuses (Abdo et al. 2010c). Moreover, multi-wavelength campaign, including γ -ray observation as well as complementary observations from radio to X rays, becomes a regular approach to investigate the physical processes of AGN jet, and γ -ray emission of blazars is observed tightly connected with emissions in other widows of the electromagnetic radiation (e.g., Marscher et al. 2008; Abdo et al. 2010d; Liao et al. 2014, 2016). In high redshift regime (i.e. $z > 2$), γ -ray variability of several blazars has been detailedly studied, including 0836+710 ($z=2.22$; Akyuz et al. 2013, TXS 0536+135 ($z=2.69$; Orienti et al. 2014), PKS 1830–211 ($z=2.51$; Abdo et al. 2015), CGRaBS J0225+1846 ($z=2.69$; Paliya et al. 2016) and PKS 2149–306 ($z=2.35$; D’Ammando & Orienti 2016). Among these sources, PKS 2149–306 and PKS 1830–211 are the most luminous ones with peaking γ -ray luminosities of 1.5×10^{50} and 2.9×10^{50} erg s^{-1} (D’Ammando & Orienti 2016; Abdo et al. 2015), respectively. Meanwhile, evidences of fast γ -ray variability have been claimed for 0836+710 and PKS 1830–211 ($\tau_{\text{doub, source}} \sim 2$ -hr; Akyuz et al. 2013; Abdo et al. 2015). By comparison, blazars beyond redshifts 3 are focused in this study. On one hand, violent γ -ray variability with large amplitude (i.e. over one order of magnitude) for NVSS J053954–283956 and NVSS J080518+614423 is reported. Especially, the former has a peaking γ -ray luminosity of 1.1×10^{50} erg s^{-1} (in this work we take a Λ CDM cosmology with $H_0 = 67 \text{ km s}^{-1} \text{ Mpc}^{-1}$, $\Omega_m = 0.32$, and $\Omega_\Lambda = 0.68$; Planck Collaboration et al. 2014), becoming the third most luminous source among the high redshift blazars and the most distant γ -ray flaring source so far. Meanwhile, the intrinsic doubling variability timescale of NVSS J053954–283956 is constrained as short as 1.4-hr,

which makes it also the most distant source with known intraday γ -ray variability up to now. The energy dissipation mechanism corresponding to this extreme phenomenon could be magnetic reconnection process and “minijets” scenario (e.g., [Giannios et al. 2009](#); [Cerutti et al. 2012](#); [Blandford et al. 2015](#)). On the other hand, our study reveals significant long-term γ -ray variability in 3 of these sources. The significant γ -ray variability together with the results of γ -ray localization analyses in the flaring epoch, strongly support the blazar nature of these γ -ray sources. Meanwhile, the observed bluer-when-brighter spectral variability behaviors suggest that identification of flaring epochs of high redshift blazars is helpful for searching the distant high energy γ -ray photons and may be used to constrain extragalactic background light (EBL) models.

Since variation of optical emissions of FSRQs has been always observed simultaneously with variation of their γ -ray emissions, we also look up into archival Palomar Transient Factory (PTF)/intermediate PTF (iPTF) data to search additional evidence of fast variability for these sources. The detailed description of the PTF/iPTF project can be found in [Rahmer et al. \(2008\)](#), and data reduction pipelines as well as photometric calibration procedures have been introduced in literature (e.g., [Law et al. 2009](#); [Ofek et al. 2012a,b](#); [Laher et al. 2014](#); [Surace et al. 2015](#)). Catalog Mould R (i.e. R_{PTF}) band **SExtractor** ([Bertin & Arnouts 1996](#)) data from the IPAC pipeline for all 7 high redshift blazars have been downloaded from the PTF/IPAC data archive hosted at the NASA/IPAC Infrared Science Archive (IRSA)⁴. The R_{PTF} mag for each source is extracted by matching the detected sources in the catalogs to the input high redshift blazar with a match radius of two arc seconds. Unfortunately, except NVSS J151002+570243 and NVSS J163547+362930, the PTF/iPTF data of these sources are rather sparse (i.e. ≤ 20 nights for 105 months). Meanwhile, the optical emission of NVSS J151002+570243 is faint (i.e. $r_{sdss} \simeq 20.3$ mag), close to the detection limit of a routine 60 s R_{PTF} band exposure (~ 21 mag; [Ofek et al. 2012a](#)). Thus only light curve of NVSS J163547+362930 is presented. The light curve is extracted by a python script⁵ with two steps. Firstly, several comparison stars (i.e. $\text{CLASS_STAR} > 0.95$ and $\text{FLAGS} = 0$) are picked under photometric condition (i.e. $\text{PHTCALFL} = 1$ and $\text{PCALRMSE} < 0.04$, 19 nights) based on their stable fluxes (i.e. $\text{mag}_{\text{std}} < 0.04$) throughout the entire time range. Then differential photometry based on these comparison stars is adopted to correct outliers affected by bad weather in “raw” light curve. As shown in Figure 8, significant variability can be directly seen in the daily averaged PTF/iPTF light curve of NVSS J163547+362930 that includes 92 nights with time range between MJD 55635.5 and MJD 56847.2. There

⁴<http://irsa.ipac.caltech.edu/applications/ptf/>

⁵An example of such a script can be found at http://phares.caltech.edu/iptf/iptf_SummerSchool_2014/Miller2_problems.html.

are four main optical flares in the light curve. Interestingly, in one flare that has well data coverage, the optical flux quickly rises from MJD 56060.4 with $R_{\text{PTF}} = 20.6$ to MJD 56065.3 with $R_{\text{PTF}} = 19.1$, indicating that the doubling time at the source frame then is ~ 12 -hr, see the zoomed-in panel of Figure 8. This intraday optical variability behavior indicates that the central engine is highly active, consistent with the sign of fast γ -ray variability based on the 15-day γ -ray light curve, though no simultaneous iPTF observation is accessible when the γ -ray flare appears.

Based on the observed fast γ -ray variability, values of the Doppler factor of emitting jet blob should be high to avoid heavy absorption on γ rays from soft photons via $\gamma\gamma$ process. The optical depth of $\gamma\gamma$ absorption can be calculated as (Dondi & Ghisellini 1995):

$$\tau_{\gamma\gamma}(x') = \frac{\sigma_{\text{T}}}{5} n'(x'_t) x'_t R', \quad (3)$$

where σ_{T} is the scattering Thomson cross section, $n'(x')$ is the number density of the target photon, x'_t is the energy of the target photon in dimensionless units, and R' is the absorption length. The soft photons can be from the jet radiation itself and external emission from the accretion system (e.g. from accretion disk or broad emissions lines). Since γ rays with energy $\simeq 3$ GeV are detected during the flaring epoch of NVSS J053954–283956 and NVSS J080518+614423, energies of absorption soft photons could be at several keV and several tens of eV for the internal and external absorption, respectively. Only the former is considered here because few information of emissions at extreme ultraviolet wavelength is known. Adopting the variability timescale of 1.4-hr and 19.6-hr for these two sources and setting L_{soft} as 10^{47} erg s^{-1} (Ghisellini et al. 2010), we have $\delta \gtrsim 11$ and $\delta \gtrsim 7$. A similar calculation can be applied on NVSS J163547+362930 ($\delta \gtrsim 7$ while $E_{\gamma} \simeq 2$ GeV) by assuming the optical and γ -ray emissions share a same radiation region. Therefore, radius of the radiation region (i.e. $R_{\gamma} < \delta c\tau_{\text{doub,source}}$) can be constrained as smaller than 1.7×10^{15} cm, 1.5×10^{16} cm and 9.1×10^{15} cm for NVSS J053954–283956, NVSS J080518+614423 and NVSS J163547+362930, respectively. The corresponding characteristic distance scale of the radiation region along the jet for a conical geometry is $r_{\gamma} \simeq R_{\gamma}/\theta \simeq R_{\gamma}\Gamma \simeq R_{\gamma}\delta$, where θ is the jet opening angle. Compared with the typical size of broad line region (i.e. ~ 0.1 pc; Tavecchio et al. 2010), the locations of γ -ray emission region of these three sources (i.e. < 0.03 pc) could be within the broad line region (BLR). Meanwhile, the total jet power required to produce such high apparent γ -ray luminosities can be estimated as $L_{\text{jet}} \simeq L_{\gamma}/(\eta_{\text{jet}}\Gamma^2)$, where η_{jet} is the jet radiative efficiency, typically ~ 0.1 (Nemmen et al. 2012), and L_{γ} are $\sim 10^{50}$ erg s^{-1} and 10^{49} erg s^{-1} corresponding to NVSS J053954–283956 and NVSS J080518+614423, respectively. Since their Eddington luminosities are given as $\sim 3 \times 10^{47}$ erg s^{-1} and 2×10^{47} erg s^{-1} (Ghisellini et al. 2010), their jet powers will exceed the Eddington luminosity if Γ of the former source is smaller than 60 while the upper limit is 25 for the other source.

It is interesting to compare our results with those from SED modelings (Ghisellini et al. 2010; Ackermann et al. 2017), though majority of the data used there are non-simultaneous. Doppler factor values of these high redshift blazars derived from the SED modelings are ~ 11 – 15 , consistent with our results. Meanwhile, similar with our results, locations of γ -ray emission region are also found within the BLR from SED modelings. Besides these approaches, direct measurements on the ejection speed of jet blob as well as the observed brightness temperature using the shortest radio variability timescale (e.g., Hovatta et al. 2009) and compared it with the theoretically expected brightness temperature assuming equipartition (i.e. $T_B = 5 \times 10^{10}$ K; Readhead 1994), can also shed lights on the Doppler factor. However, these high redshift blazars are not included in current VLBA and radio flux monitoring projects (e.g., Lister et al. 2009; Richards et al. 2011; Jorstad et al. 2017). Nevertheless, let us make a comparison between our high redshift blazars and those at low redshifts. MOJAVE parsec-scale kinematics VLBA observations give an averaged apparent jet speed $\beta_{app} \simeq 9$ of their sample (Lister et al. 2013). Especially, observed β_{app} of bright sources with detection of fast γ -ray variability are larger than 10 (Jorstad et al. 2005). Based on multiwavelength radio light curves, a mean value of the Doppler factor for F-GAMMA FSRQs is suggested as ~ 12 (Liodakis et al. 2017). These indications from radio observations are confirmed by SED modeling studies (e.g., Ghisellini & Tavecchio 2015; Zhang et al. 2015). Meanwhile, studies of the luminosity functions of blazars and their parent populations allow for a constraint of the Doppler factor, which is in agreement with the kinematics radio observations (e.g., Ajello et al. 2012). In conclusion, no significant difference of the Doppler factor between these 7 high redshift blazars (i.e. $z > 3$) and ones nearby is found, and future simultaneous multiwavelength campaigns are helpful to further understand these highly active monsters.

According to the *Swift*-BAT detected high redshift blazars (Ajello et al. 2009), the number of SDSS-FIRST detected jetted AGN with $z > 3$ is fairly less than the expectation of the orientation based AGN unified scheme (Volonteri et al. 2011). One possible explanation is that the averaged Lorentz factor of these *Swift*-BAT high redshift blazars (i.e. $\Gamma \sim 5$) is generally lower than a routine value (i.e. $\Gamma \sim 15$). Violent and rapid variability in blazars beyond redshift 3 are found in this study. Note that in addition to the two detections of FSRQs γ -ray variability with timescale of several minutes based on either IACT observation or ToO repointing observation from *Fermi*-LAT (Aleksić et al. 2011; Ackermann et al. 2016), there are only a few FSRQs whose minimum variability is ~ 1 - 2 hrs (e.g., Saito et al. 2013; Foschini et al. 2013; Liao & Bai 2015; Hayashida et al. 2015; Liao et al. 2016). NVSS J053954–283956 is one of most violently active γ -ray FSRQs. Meanwhile, the light curves extracted here is under the survey mode operation of *Fermi*-LAT, due to the limited exposure time, the reported doubling timescales should be treated as upper limits only. Moreover,

besides NVSS J053954–283956, intraday variations are detected in other two high redshift blazars (i.e. three in all seven), which suggests that such a phenomenon should not be rare for these sources. Therefore, this deficit could be due to selection effects rather than a gradient descent of averaged Lorentz factor of blazars at higher redshifts.

We appreciate helpful suggestions from the anonymous referee. This research has made use of data obtained from the High Energy Astrophysics Science Archive Research Center (HEASARC), provided by NASA’s Goddard Space Flight Center. This research has also made use of the NASA/IPAC Extragalactic Database and the NASA/IPAC Infrared Science Archive which are operated by the Jet Propulsion Laboratory, California Institute of Technology, under contract with the National Aeronautics and Space Administration. This research makes use of the SIMBAD database, operated at CDS, Strasbourg, France.

This work was supported in part by the National Basic Research Program of China (No. 2013CB837000), NSFC under grants 11525313 (i.e., Funds for Distinguished Young Scholars) and 11703093.

REFERENCES

- Abdo, A. A., Ackermann, M., Ajello, M., et al. 2010a, *ApJ*, 715, 429
- Abdo, A. A., Ackermann, M., Ajello, M., et al. 2010b, *ApJS*, 188, 405
- Abdo, A. A., Ackermann, M., Ajello, M., et al. 2010c, *ApJ*, 710, 1271
- Abdo, A. A., Ackermann, M., Ajello, M., et al. 2010d, *Nature*, 463, 919
- Abdo, A. A., Ackermann, M., Ajello, M., et al. 2015, *ApJ*, 799, 143
- Acerro, F., Ackermann, M., Ajello, M., et al. 2015, *ApJS*, 218, 23
- Acerro, F., Ackermann, M., Ajello, M., et al. 2016, *ApJS*, 223, 26
- Ackermann, M., Ajello, M., Albert, A., et al. 2015, *ApJ*, 813, L41
- Ackermann, M., Anantua, R., Asano, K., et al. 2016, *ApJ*, 824, L20
- Ackermann, M., Ajello, M., Baldini, L., et al. 2017, *ApJ*, 837, L5
- Afonso, J., Casanellas, J., Prandoni, I., et al. 2015, *Advancing Astrophysics with the Square Kilometre Array (AASKA14)*, 71
- Aharonian, F., Akhperjanian, A. G., Bazer-Bachi, A. R., et al. 2007, *ApJ*, 664, L71

- Ajello, M., Costamante, L., Sambruna, R. M., et al. 2009, *ApJ*, 699, 603
- Ajello, M., Shaw, M. S., Romani, R. W., et al. 2012, *ApJ*, 751, 108
- Akyuz, A., Thompson, D. J., Donato, D., et al. 2013, *A&A*, 556, A71
- Alam, S., Albareti, F. D., Allende Prieto, C., et al. 2015, *ApJS*, 219, 12
- Albert, J., Aliu, E., Anderhub, H., et al. 2007, *ApJ*, 669, 862
- Aleksić, J., Antonelli, L. A., Antoranz, P., et al. 2011, *ApJ*, 730, L8
- Arlen, T., Aune, T., Beilicke, M., et al. 2013, *ApJ*, 762, 92
- Atwood, W. B., Abdo, A. A., Ackermann, M., et al. 2009, *ApJ*, 697, 1071
- Baumgartner, W. H., Tueller, J., Markwardt, C. B., et al. 2013, *ApJS*, 207, 19
- Becker, R. H., White, R. L., & Edwards, A. L. 1991, *ApJS*, 75, 1
- Begelman, M. C., Fabian, A. C., & Rees, M. J. 2008, *MNRAS*, 384, L19
- Bertin, E., & Arnouts, S. 1996, *A&AS*, 117, 393
- Blandford, R. D., & Rees, M. J. 1978, in *Pittsburgh Conference on BL Lac Objects*, ed. A. M. Wolfe (Pittsburgh, PA: Univ. Pittsburgh Press), 328
- Blandford, R. D., Yuan, Y., & Zrake, J. 2015, *American Astronomical Society Meeting Abstracts*, 225, 214.07
- Błażejowski, M., Sikora, M., Moderski, R., & Madejski, G. M. 2000, *ApJ*, 545, 107
- Bolton, J. G., Shimmins, A. J., & Wall, J. V. 1975, *Australian Journal of Physics Astrophysical Supplement*, 34, 1
- Bottacini, E., Ajello, M., et al. 2010, *A&A*, 509A, 69B
- Cerutti, B., Werner, G. R., Uzdensky, D. A., & Begelman, M. C. 2012, *ApJ*, 754, L33
- Cheung, C. C. 2017, *ATel*, 10356, 1C
- Condon, J. J., Cotton, W. D., Greisen, E. W., et al. 1998, *AJ*, 115, 1693
- D’Abrusco, R., Massaro, F., Ajello, M., et al. 2012, *ApJ*, 748, 68
- D’Ammando, F., & Orienti, M. 2016, *MNRAS*, 455, 1881

- Dermer, C. D., & Schlickeiser, R. 1993, *ApJ*, 416, 458
- Dondi, L., & Ghisellini, G. 1995, *MNRAS*, 273, 583
- Fabian, A. C. 2012, *ARA&A*, 50, 455
- Flesch, E. W. 2015, *PASA*, 32, e010
- Foschini, L., Ghisellini, G., Tavecchio, F., Bonnoli, G., & Stamerra, A. 2011, *A&A*, 530, A77
- Foschini, L., Bonnoli, G., Ghisellini, G., et al. 2013, *A&A*, 555, A138
- Gehrels, N., Chincarini, G., Giommi, P., et al. 2004, *ApJ*, 611, 1005
- Giannios, D., Uzdensky, D. A., & Begelman, M. C. 2009, *MNRAS*, 395, L29
- Ghisellini, G., Della Ceca, R., Volonteri, M., et al. 2010, *MNRAS*, 405, 387
- Ghisellini, G., Sbarrato, T., Tagliaferri, G., et al. 2014, *MNRAS*, 440, L111
- Ghisellini, G., & Tavecchio, F. 2015, *MNRAS*, 448, 1060
- Griffith, M., Langston, G., Hefflin, M., et al. 1990, *ApJS*, 74, 129
- Hayashida, M., Nalewajko, K., Madejski, G. M., et al. 2015, *ApJ*, 807, 79
- Hovatta, T., Valtaoja, E., Tornikoski, M., & Lähteenmäki, A. 2009, *A&A*, 494, 527
- Jorstad, S. G., Marscher, A. P., Lister, M. L., et al. 2005, *AJ*, 130, 1418
- Jorstad, S. G., Marscher, A. P., Morozova, D. A., et al. 2017, *ApJ*, 846, 98
- Laher, R. R., Surace, J., Grillmair, C. J., et al. 2014, *PASP*, 126, 674
- Law, N. M., Kulkarni, S. R., Dekany, R. G., et al. 2009, *PASP*, 121, 1395
- Liao, N. H., Bai, J. M., Liu, H. T., et al. 2014, *ApJ*, 783, 83
- Liao, N. H., & Bai, J. M. 2015, *New A*, 34, 134
- Liao, N.-H., Xin, Y.-L., Fan, X.-L., et al. 2016, *ApJS*, 226, 17
- Liodakis, I., Marchili, N., Angelakis, E., et al. 2017, *MNRAS*, 466, 4625
- Lister, M. L., Aller, H. D., Aller, M. F., et al. 2009, *AJ*, 137, 3718-3729
- Lister, M. L., Aller, M. F., Aller, H. D., et al. 2013, *AJ*, 146, 120

- Maraschi, L., Ghisellini, G., & Celotti, A. 1992, *ApJ*, 397, L5
- Marscher, A. P., Jorstad, S. G., D’Arcangelo, F. D., et al. 2008, *Nature*, 452, 966
- Mattox, J. R., Bertsch, D. L., Chiang, J., et al. 1996, *ApJ*, 461, 396
- Mattox, J. R., Wagner, S. J., Malkan, M., et al. 1997, *ApJ*, 476, 692
- Morganti, R., Fogasy, J., Paragi, Z., Oosterloo, T., & Orienti, M. 2013, *Science*, 341, 1082
- Nemmen, R. S., Georganopoulos, M., Guiriec, S., et al. 2012, *Science*, 338, 1445
- Nolan, P. L., Abdo, A. A., Ackermann, M., et al. 2012, *ApJS*, 199, 31
- Ofek, E. O., Laher, R., Surace, J., et al. 2012a, *PASP*, 124, 62
- Ofek, E. O., Laher, R., Surace, J., et al. 2012b, *PASP*, 124, 854
- Orienti, M., D’Ammando, F., Giroletti, M., et al. 2014, *MNRAS*, 444, 3040
- Pâris, I., Petitjean, P., Aubourg, É., et al. 2014, *A&A*, 563, A54
- Paliya, V. S., Parker, M. L., Fabian, A. C., & Stalin, C. S. 2016, *ApJ*, 825, 74
- Planck Collaboration, Ade, P. A. R., Aghanim, N., et al. 2014, *A&A*, 571, A16
- Rahmer, G., Smith, R., Velur, V., et al. 2008, *Proc. SPIE*, 7014, 70144Y
- Readhead, A. C. S. 1994, *ApJ*, 426, 51
- Richards, J. L., Max-Moerbeck, W., Pavlidou, V., et al. 2011, *ApJS*, 194, 29
- Romani, R. W., Sowards-Emmerd, D., Greenhill, L., & Michelson, P. 2004, *ApJ*, 610, L9
- Romani, R. W. 2006, *AJ*, 132, 1959
- Sambruna, R. M., Tavecchio, F., Ghisellini, G., et al. 2007, *ApJ*, 669, 884
- Saito, S., Stawarz, Ł., Tanaka, Y. T., et al. 2013, *ApJ*, 766, L11
- Sbarrato, T., Ghisellini, G., Nardini, M., et al. 2012, *MNRAS*, 426, L91
- Sikora, M., Begelman, M. C., & Rees, M. J. 1994, *ApJ*, 421, 153
- Snellen, I. A. G., McMahon, R. G., Hook, I. M., & Browne, I. W. A. 2002, *MNRAS*, 329, 700

- Sowards-Emmerd, D., Romani, R. W., Michelson, P. F., Healey, S. E., & Nolan, P. L. 2005, *ApJ*, 626, 95
- Surace, J., Laher, R., Masci, F., Grillmair, C., & Helou, G. 2015, *Astronomical Data Analysis Software and Systems XXIV (ADASS XXIV)*, 495, 197
- Tavecchio, F., Ghisellini, G., Bonnoli, G., & Ghirlanda, G. 2010, *MNRAS*, 405, L94
- Torrealba, J., Chavushyan, V., Cruz-González, I., et al. 2012, *Rev. Mexicana Astron. Astrofis.*, 48, 9
- Ulrich, M.-H., Maraschi, L., & Urry, C. M. 1997, *ARA&A*, 35, 445
- Urry, C. M., & Padovani, P. 1995, *PASP*, 107, 803
- Volonteri, M. 2010, *A&A Rev.*, 18, 279
- Volonteri, M., Haardt, F., Ghisellini, G., Della Ceca, R. 2011. *MNRAS*, 416, 216
- Vovk, I., & Neronov, A. 2013, *ApJ*, 767, 103
- Wehrle, A. E., Pian, E., Urry, C. M., et al. 1998, *ApJ*, 497, 178
- Wright, A. E., Peterson, B. A., Jauncey, D. L., & Condon, J. J. 1978, *ApJ*, 226, L61
- Wright, E. L., Eisenhardt, P. R. M., Mainzer, A. K., et al. 2010, *AJ*, 140, 1868
- Yi, W.-M., Wang, F., Wu, X.-B., et al. 2014, *ApJ*, 795, L29
- York, D. G., Adelman, J., Anderson, J. E., Jr., et al. 2000, *AJ*, 120, 1579
- Zhang, J., Xue, Z.-W., He, J.-J., Liang, E.-W., & Zhang, S.-N. 2015, *ApJ*, 807, 51
- Zhang, P.-f., Yan, D.-h., Liao, N.-h., & Wang, J.-c. 2017, *ApJ*, 835, 260
- Zamorani, G., Henry, J. P., Maccacaro, T., et al. 1981, *ApJ*, 245, 357

Table 1. Basic information and γ -ray properties of the known 7 γ -ray blazars beyond redshift 3.

NVSS name	b	z	$F_{1.4 \text{ GHz}}$	R_{mag}	$M_{BH,\odot}$	F_γ	Γ_γ	TS	σ_{var}
J053954–283956	-27.3°	3.1	0.86	19.0	9.3	4.92 ± 0.23	2.80 ± 0.04	1737.8	15.7
J064632+445116	17.5°	3.4	0.45	18.5	9.1	1.35 ± 0.19	2.95 ± 0.13	103.3	1.2
J080518+614423	32.4°	3.0	0.83	19.6	9.07	2.21 ± 0.13	2.83 ± 0.05	467.2	10.8
J135406–020603	50.1°	3.7	0.73	19.2	8.9	1.0 ± 0.16	2.83 ± 0.13	60.1	5.0
J151002+570243	50.3°	4.3	0.20	19.9	8.5	0.42 ± 0.13	2.72 ± 0.20	32.7	3.2
J163547+362930	42.1°	3.6	0.15	20.6	8.7	1.93 ± 0.29	3.21 ± 0.12	129.9	6.2
J212912–153841	-41.9°	3.3	0.59	16.5	9.8	1.62 ± 0.19	3.04 ± 0.12	108.9	2.4

Note. — (1) NVSS name of the object; (2) Galactic latitude; (3) redshift; (4) NVSS radio flux density at 1.4 GHz in Jy; (5) apparent R band magnitude; (6) logarithm of black hole mass; (7) average γ -ray flux of 105 months LAT data analysis in scale of 10^{-8} ph cm $^{-2}$ s $^{-1}$; (8) γ -ray spectral index corresponding to col. (7); (9) TS value corresponding to col. (7); (10) significance of the variability estimated from the monthly γ -ray light curve. The Galactic latitudes are derived from NED. The redshifts and the R magnitudes are obtained from Half Million Quasars catalog (Flesch 2015). The NVSS 1.4 GHz flux densities are from Condon et al. (1998). Note that the σ_{var} here for NVSS J163547+362930 could be influenced by the neighbor 3FGL J1635.2+3809. More details see Section 3.2.1.

Table 2. Flux doubling timescales

NVSS Name	Epoch	Time bin	$\tau_{doub,source}$ (hour)	p-value
J053954–283956	flare-C	3-day	8.3 ± 0.2	2.9×10^{-50}
J053954–283956	flare-C	12-hour	2.4 ± 0.6	7.0×10^{-8}
J053954–283956	flare-C	6-hour	1.3 ± 0.3	1.6×10^{-5}
J053954–283956	flare-C	3-hour	1.5 ± 0.6	0.11
J080518+614423	flare-A	3-day	19.6 ± 2.5	1.0×10^{-27}

Note. — (1) NVSS name of the object; (2) Data time epoch given in Figure 1; (3) Estimated doubling timescales at the source frame along with 1σ errors; (4) Probability that the null hypothesis stands.

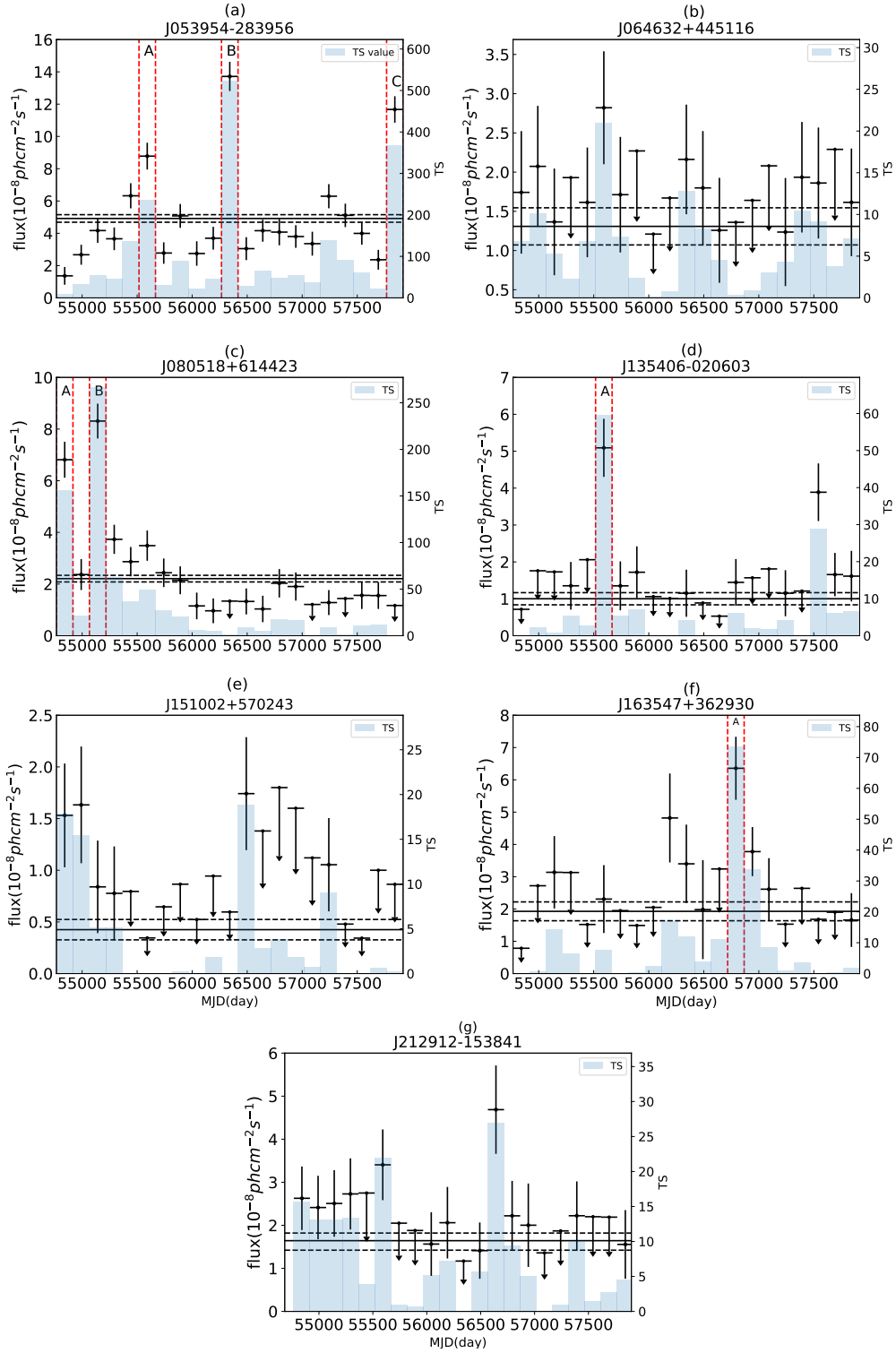


Fig. 1.— 100 MeV - 100 GeV monthly light curves of 7 high-redshift γ -ray blazars. Horizontal solid line along with two dashed lines in each panel represent the average flux and its 1σ error range derived in the global analysis, respectively. Red dashed vertical lines represent time epochs when further temporal analyses are performed. If any significant γ -ray flares appear, they are marked as different capitals.

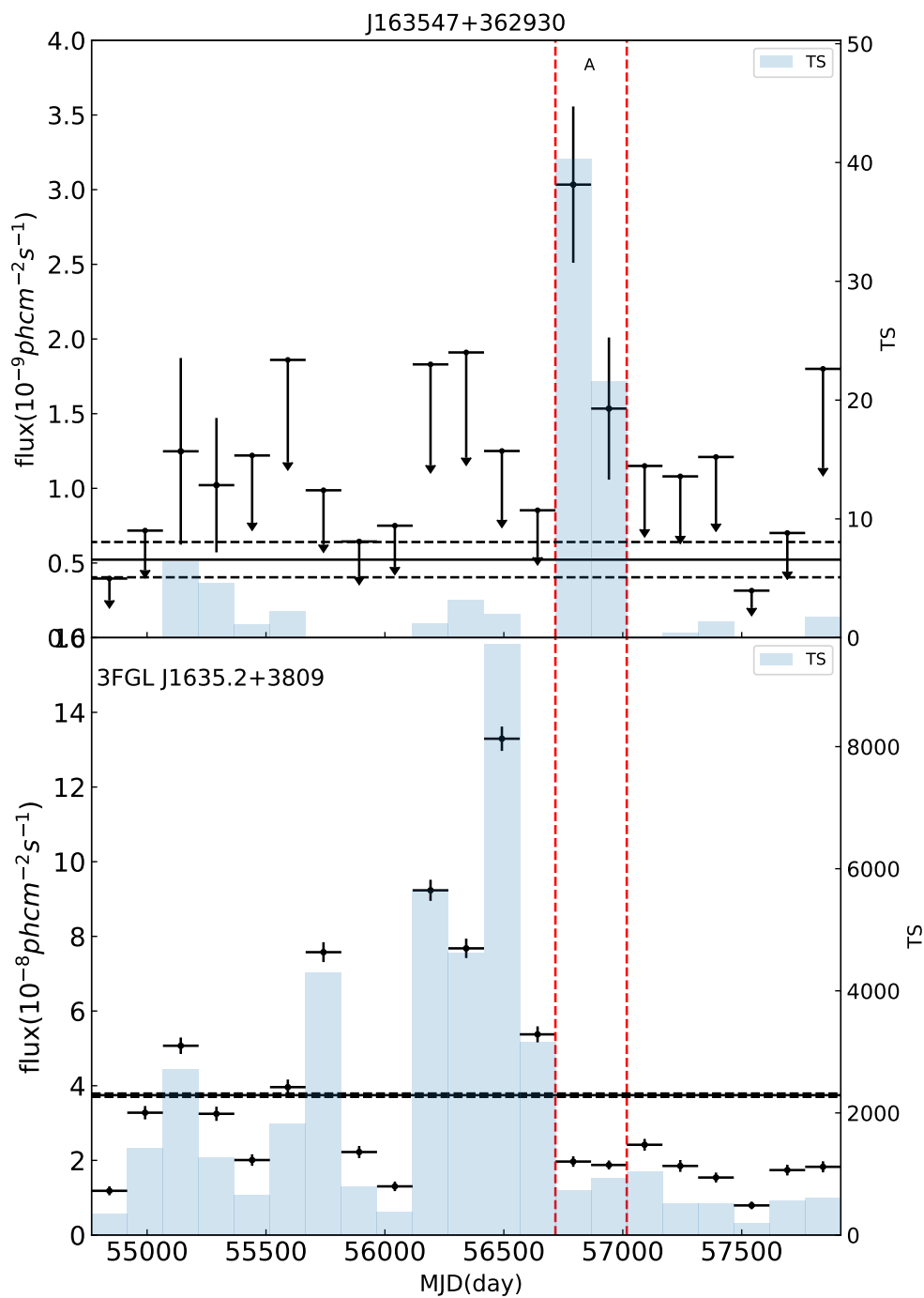


Fig. 2.— 500 MeV - 100 GeV monthly light curve of NVSS J163547+362930 as well as its neighbor 3FGL J1635.2+3809. Horizontal solid line and two dashed lines in each panel represent the average flux and its 1σ error range derived in the global analysis, respectively. Red dashed vertical lines represent the time epoch when the 15-day bin light curves are extracted.

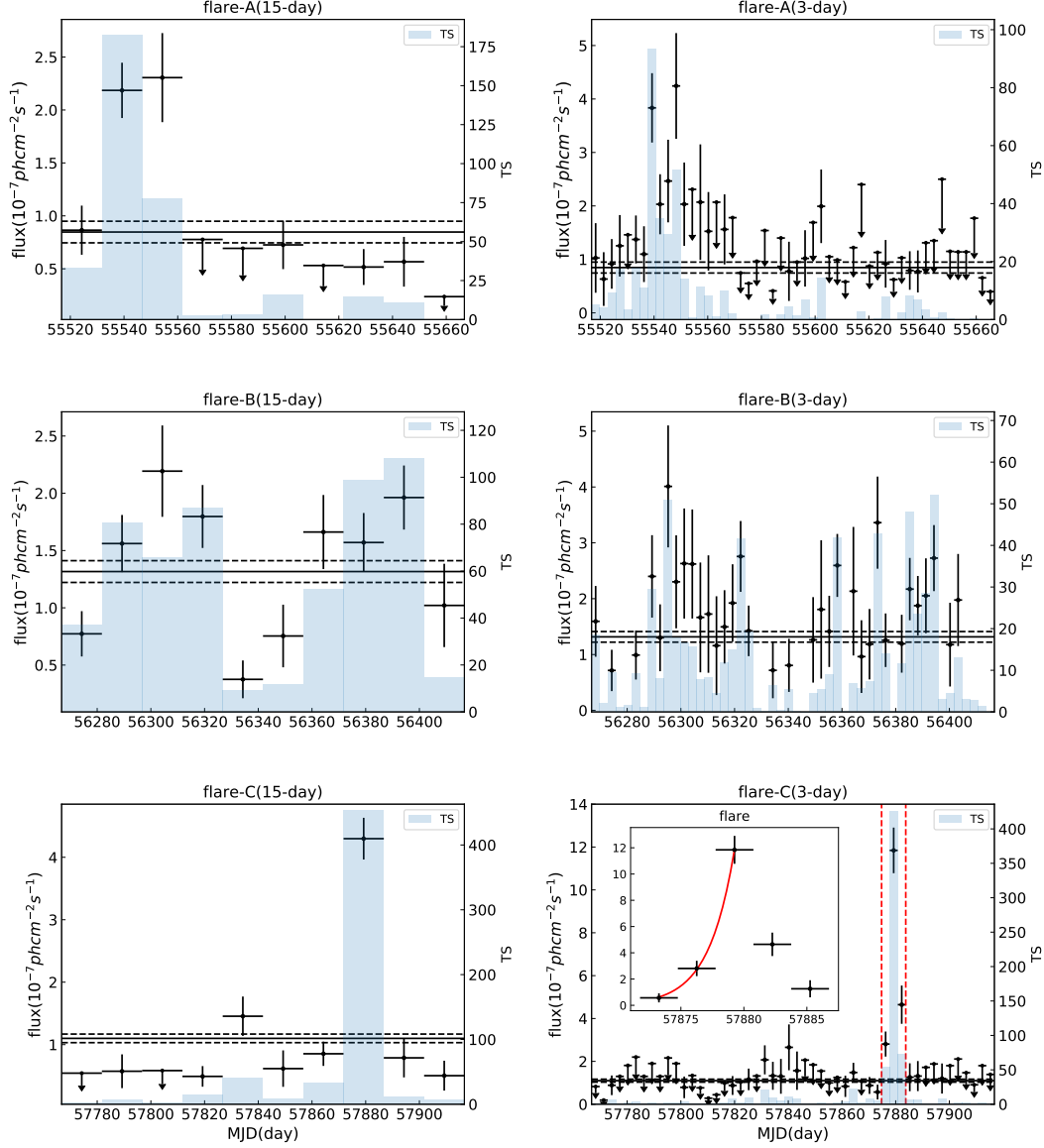


Fig. 3.— 15-day and 3-day time bin light curves correspond to the three flares of NVSS J053954–283956. Horizontal solid line along with two dashed lines in each panel represent the average flux and its 1σ error range then. In the 3-day time bin light curve of flare-C (i.e. the right bottom panel), red dashed vertical lines represent the time epoch when searches of intraday γ -ray variability are performed. Meanwhile, a zoomed-in panel of flare-C along with an exponential fit (red solid line) of the ascent phase is also presented here.

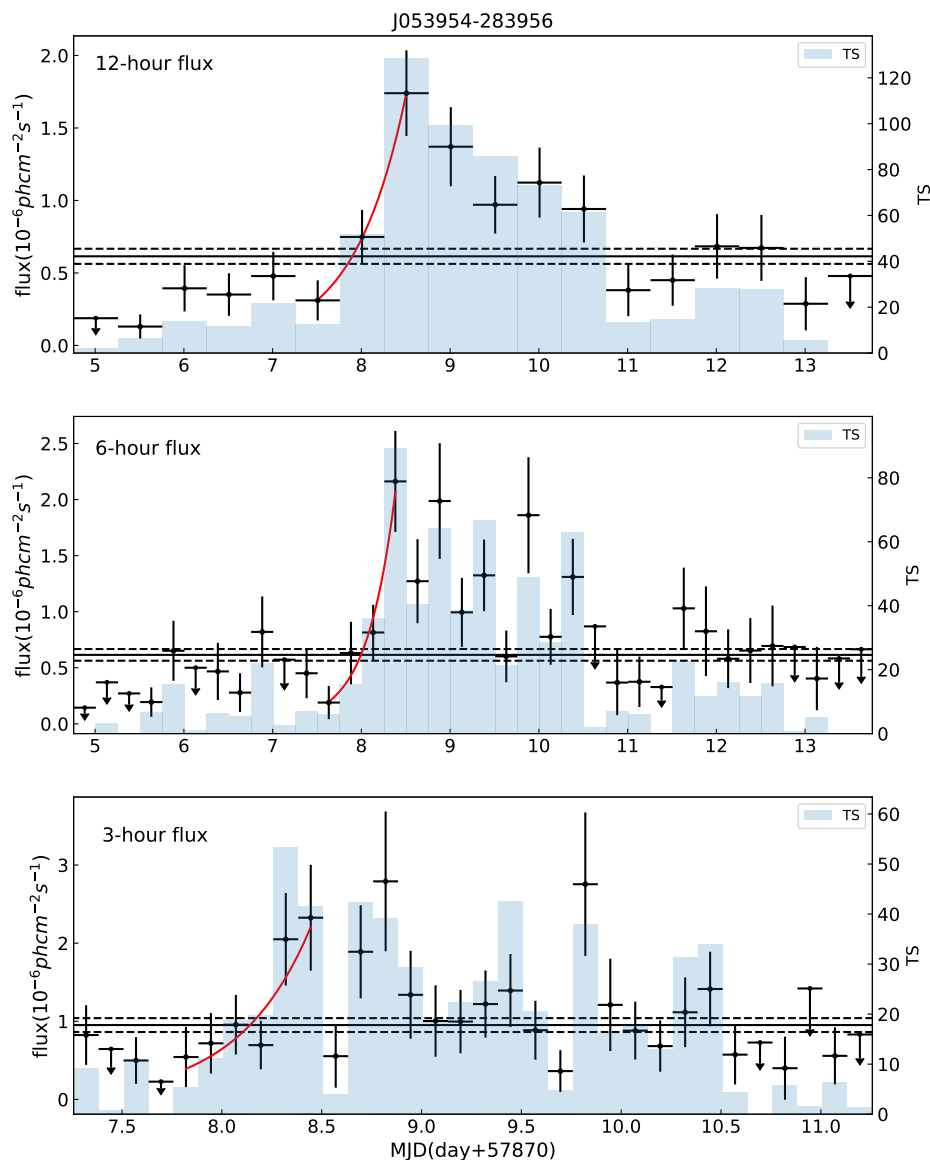


Fig. 4.— 12-hr (upper panel), 6-hr (middle panel) and 3-hr (bottom panel) light curves focusing on the flare-C of NVSS J053954–283956. Horizontal solid line as well as two dashed lines in each panel correspond to the average flux and its 1σ error range then. Red lines represent the exponential fits of the ascent phase of flare-C.

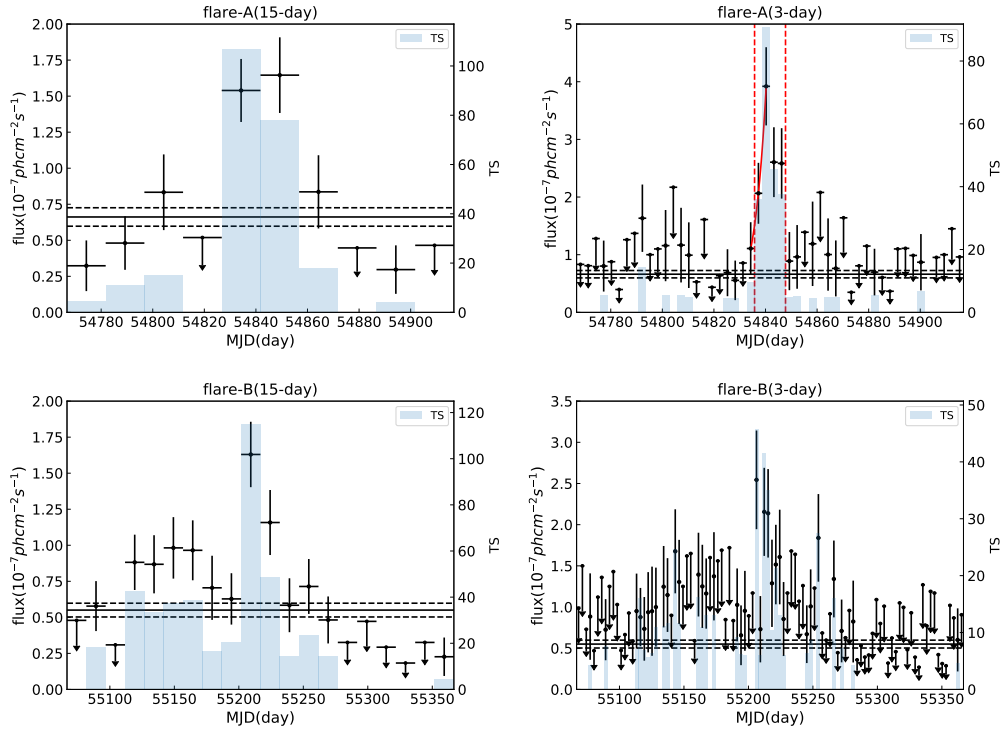


Fig. 5.— 15-day and 3-day time bin light curves correspond to the two flares of of NVSS J080518+614423. Horizontal solid line along with two dashed lines in each panel represent the average flux and its 1σ error range then. In the 3-day time bin light curve of flare-A (i.e. the right upper panel), red dashed vertical lines represent the time epoch when further temporal analyses are performed, along with an exponential fit (red solid line) of the ascent phase.

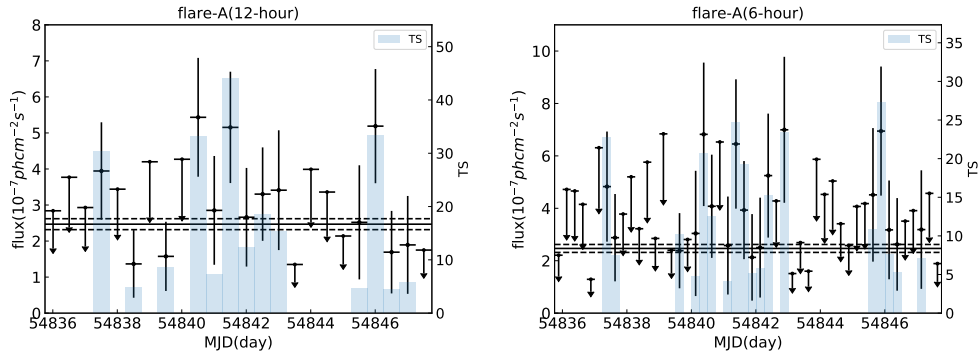


Fig. 6.— 12-hr (left panel) and 6-hr (right panel) light curves focusing on the flare-A epoch of NVSS J080518+614423. Horizontal solid line as well as two dashed lines in each panel correspond to the average flux and its 1σ error range then.

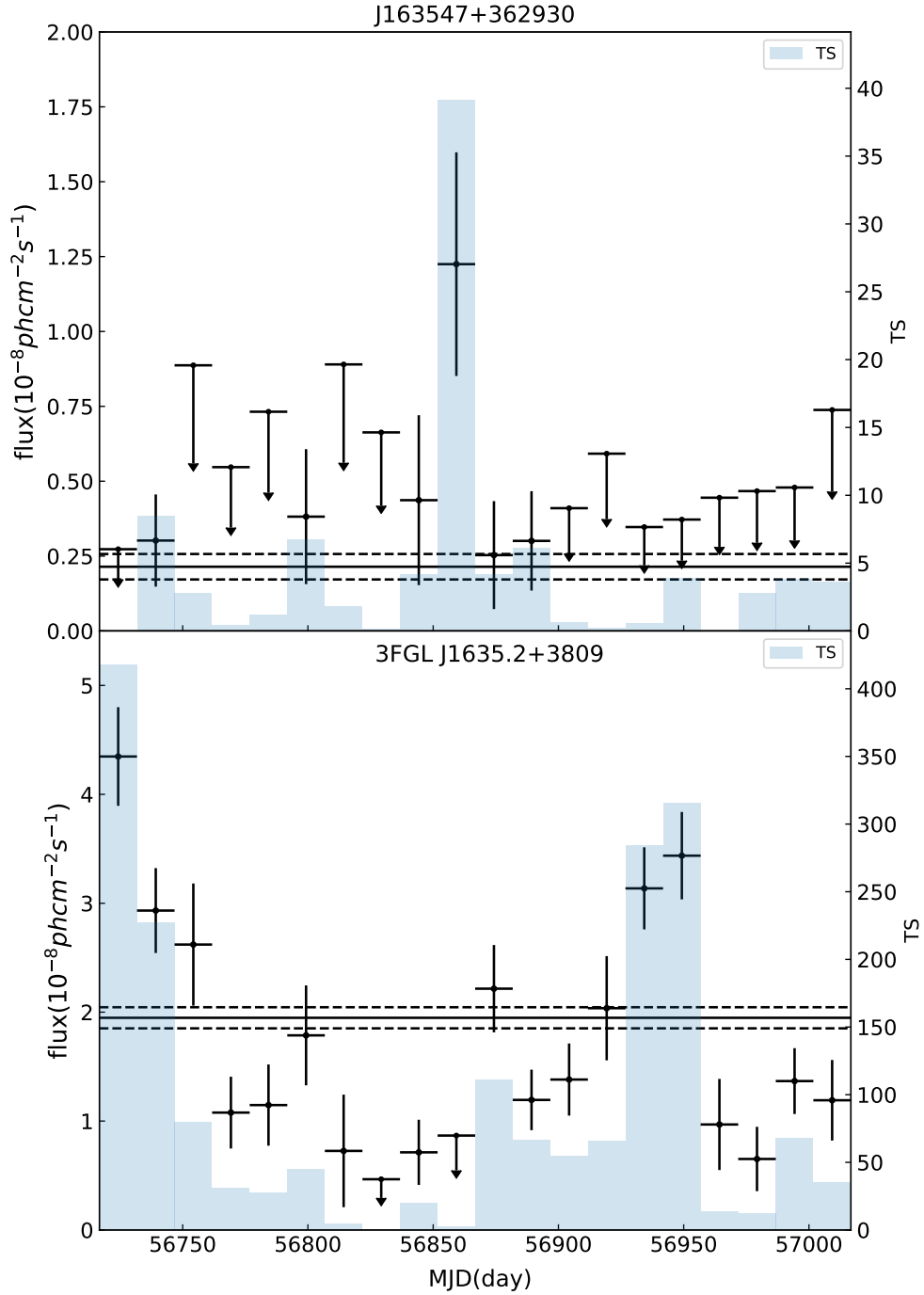


Fig. 7.— 500 MeV - 100 GeV 15-day time bin light curves of NVSS J163547+362930 as well as its neighbor 3FGL J1635.2+3809 focusing the flare-A epoch of the target. Horizontal solid line and two dashed lines in each panel represent the average flux and its 1σ error range of these two sources then.

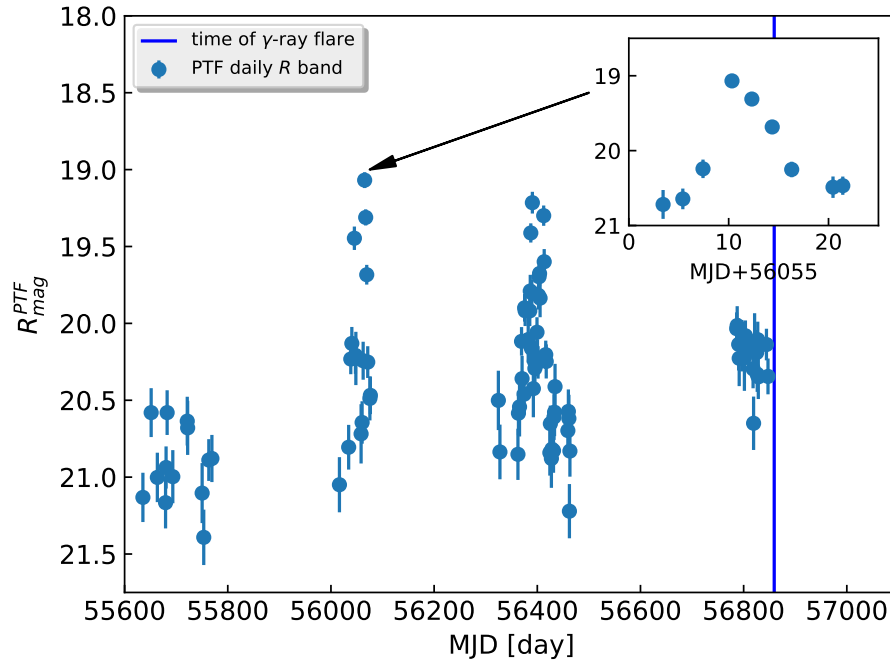


Fig. 8.— Daily PTF/iPTF optical light curve of NVSS J163547+362930 with a zoomed-in panel of a flare peaking at MJD 55065.3.